

Landau levels and magneto-optical responses in Weyl semimetal quantum wells in a non-uniform magnetic field

Le T. Hoa,¹ Le T. T. Phuong ^{1,2}, S. S. Kubakaddi,³ Nguyen N. Hieu ^{4,5} and Huynh V. Phuc ^{6,*}

¹Department of Physics, University of Education, Hue University, Hue 530000, Vietnam

²Center for Theoretical and Computational Physics, University of Education, Hue University, Hue 530000, Vietnam

³Department of Physics, K. L. E. Technological University, Hubballi-580 031, Karnataka, India

⁴Institute of Research and Development, Duy Tan University, Da Nang 550000, Vietnam

⁵Faculty of Natural Sciences, Duy Tan University, Da Nang 550000, Vietnam

⁶Division of Theoretical Physics, Dong Thap University, Cao Lanh 870000, Vietnam



(Received 30 June 2022; accepted 5 August 2022; published 15 August 2022)

We study the Landau level (LL) structure and magneto-optical responses in the Weyl semimetal (WSM) quantum well in the presence of a non-uniform magnetic field (NUMF). The number of LLs in the NUMF is found to be finite, and the LL structure of the system is significantly affected by the inhomogeneity of the magnetic field. The added electric field significantly affects the separation of the two Weyl nodes in momentum space. We investigate the role of the inhomogeneity of the magnetic field, temperature, electron density, and electric field, as well as the doping level on the optical response properties. Both longitudinal and Hall susceptibilities in the (x, y) plane and the longitudinal susceptibility in the z direction display a series of peaks whose height and spacing decrease with the increase of the LL index. At $T \neq 0$, thermal excitation triggers new transitions, which are forbidden by the Pauli blocked at $T = 0$. The optical response spectra are different when the chemical potential lies in different energy regions, which are strongly dependent on the inhomogeneity of the magnetic field, electron density, and electric field. In this paper, we provide a possible way to control the optical response spectrum in WSM materials by changing these parameters.

DOI: [10.1103/PhysRevB.106.075412](https://doi.org/10.1103/PhysRevB.106.075412)

I. INTRODUCTION

A Weyl semimetal (WSM) is an interesting material class whose low energy is described as massless chiral fermions, named *Weyl fermions*. WSMs have been demonstrated to be charged even at room temperatures [1–3] and are a critical topological phase of matter in addition to topological insulators [4]. The low-energy bands of WSMs have also displayed a linear dispersion whose conduction and valence bands touch each other at isolated Dirac points, named *Weyl nodes*. These nodes always appear in pairs and have opposite chiralities, acting as the beginning and end points of the Berry curvature in the momentum space [5,6]. In WSMs, both inversion and time-reversal symmetries or either one of them is broken [1,7]. If both of these symmetries are protected, Weyl nodes will be degenerated [8], and the system should be referred to as a *Dirac semimetal* whose typical representatives are Na_3Bi [9] or Cd_3As_2 [10]. Recently, a WSM has been predicted theoretically [11,12] and observed experimentally in TaAs [13]. This material is expected to have many useful applications in electronics and computing due to its high mobility of charged Weyl fermions [14].

When a uniform magnetic field (UMF) is applied to the system, the linear dispersion electronic states are quantized to a set of discrete energy levels, which has been observed in

Cd_3As_2 [15]. Studying the optical transitions between these Landau levels (LLs) allows us to determine the distance between the LLs, thereby defining the characteristics of fermions in the materials [5,16–21]. The optical conductivity in an isolated Weyl node is shown as a series of asymmetric peaks both without [16] and with quadratic terms [17]. The magneto-response in the z direction has been found to be comparable with that in the (x, y) plane [5]. Along with this, the existence of a chiral anomaly [22] sets WSMs apart from other two-dimensional (2D) monolayer materials [23–29]. The electronic properties of the WSM in the presence of a UMF have been studied in great detail using a minimal model [5,18,30]. However, the effects of the non-UMF (NUMF) on the wave functions, the energy spectrum, and the magneto-optical properties of the WSM have not yet received sufficient research attention.

It is well known that, in the NUMF case, the energy spectrum and wave function have many different characteristics in comparison with those in the UMF one [31]. Theoretically, different kinds of NUMFs have been studied in 2D electron gas [32,33]. Experimental strategies for creating such NUMFs can be found in a review by Nogaret [34]. According to that, such NUMFs can be implemented by using micromagnetic, superconducting elements, and non-planar 2D electron gas. While a microscopical NUMF can be obtained by fabricating micromagnets in the proximity of a 2D electron gas, superconducting elements [35] could be used to screen applied magnetic fields using the Meissner effect [34]. Another type

*Corresponding author: hvphuc@dthu.edu.vn

of NUMF is the magnetic step, which can be obtained by overgrowing heterojunctions on a non-planar substrate [36]. The magnetic field generated by this system will have the following characteristic: It has a finite value at the facet and is zero everywhere else.

Among different types of NUMF, the exponentially decaying magnetic field (EDMF) is one of the most popular [37,38], where the analytic solutions for a Dirac electron have been obtained in several systems such as quantum wells (QWs) [39], monolayer graphene [31,40], bilayer graphene [41], and monolayer black phosphorus [42]. According to that, the wave functions of electrons in the EDMF are not expressed by Hermite polynomials but by Laguerre polynomials, and the number of their corresponding LLs energies is finite. Thus, the magneto-optical response properties of the systems placed in the EDMF have many interesting features and need to be studied in more detail. Such an EDMF can be produced by parallelly applying a UMF to one planar surface of a superconductor. Then an EDMF will occur inside the superconductor within the penetration depth λ [39,41,42]. This design can be used to consider a NUMF in our system.

In this paper, we present a calculation of the susceptibilities of a WSM QW in the presence of a NUMF. We study the contribution of the electric field to the energy spectrum of WSM, which is described by a two-node model [5,18,30]. It has been shown that the distance between the two Weyl nodes is significantly dependent on the electric field. We study the influence of the temperature, the magnetic field penetration, electron density, the electric field, and polarization orientation of the light on the longitudinal and Hall susceptibilities in the (x, y) plane and in the z direction in both cases of doped and undoped WSMs.

II. MODEL AND FORMALISM

A. Minimal model

We start with the Hamiltonian by the minimal model for a WSM [5,18,30]:

$$\mathcal{H}_0 = \hbar v_F(k_x \sigma_x + k_y \sigma_y) + M_a(k_c^2 - k^2) \sigma_z, \quad (1)$$

where v_F is the Fermi velocity in the (x, y) plane with $\hbar v_F = 2.5$ eV Å; $k = |\mathbf{k}|$ with $\mathbf{k} = (k_x, k_y, k_z)$ being the wave vector; σ_x , σ_y , and σ_z are the Pauli matrices; and $k_c = 0.1$ Å⁻¹ and $M_a = 10$ eV Å² are the model parameters [18]. Applying a uniform electric field $\mathbf{E} = (0, 0, -E_z)$ to the system, the dispersion of energy bands of the system is found to be

$$E_{\pm} = \pm \sqrt{(\hbar v_F)^2(k_x^2 + k_y^2) + [M_a(k_c^2 - k^2) - \Delta_z]^2}, \quad (2)$$

where $\Delta_z = eE_z L_z$, with L_z being the length of the system in the z direction. At $k_x = k_y = 0$, the energy dispersion in Eq. (2) reduces to $E_{\pm} = \pm |M_0(k_c^2 - k_z^2) - \Delta_z|$. In Fig. 1, we show the energy spectrum as a function of k_z at $k_x = k_y = 0$ for different values of the electric field, which is described through a dimensionless parameter $\gamma = \Delta_z / (M_a k_c^2)$. In the absence of electric field, $\gamma = 0$ [see Fig. 1(a)], the two bands E_+ and E_- intersect at two nodes $(0, 0, \pm k_c)$. In the range between the two nodes, i.e., $-k_c < k_z < k_c$, the WSM displays a topological phase [5,18], like that observed in silicene [43,44]. When the electric field is increased such that $\gamma < 1$

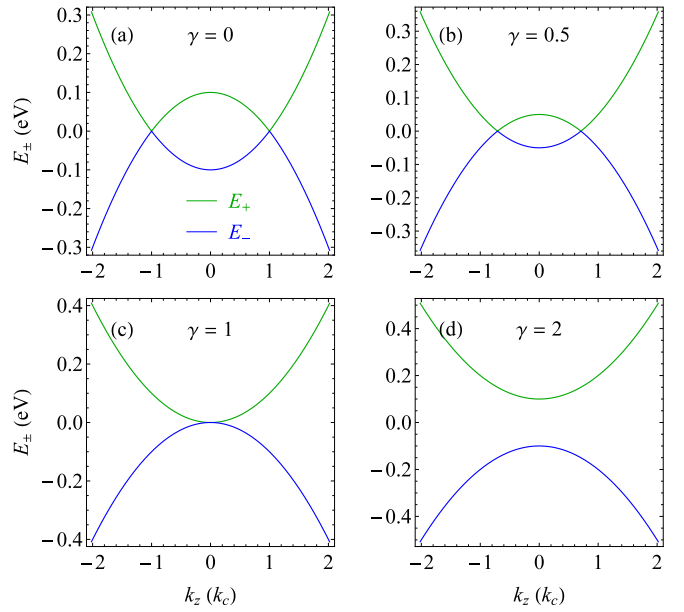


FIG. 1. Energy spectrum as a function of k_z at $k_x = k_y = 0$ for different electric fields ($\Delta_z = \gamma M_a k_c^2$). (a)–(d) are for $\gamma = 0, 0.5, 1$, and 2, respectively.

[see Fig. 1(b)], the system remains in a topological phase but with the intersections being changed to $k_z = \pm k_a$ with $k_a = (k_c^2 - \Delta_z / M_a)^{1/2} = k_c(1 - \gamma)^{1/2}$. This topological property can be characterized through the nonzero Chern number [45], which is nonzero (zero) in (out of) the range of $-k_a < k_z < k_a$ [46]. When $\gamma = 1$ [see Fig. 1(c)], the two nodes are converged into one, the two bands intersect at only one node, and the system displays a special type of phase, which is related to the valley-polarized metal phase in silicene [47]. As γ continues increasing further with $\gamma > 1$ [see Fig. 1(d)], the two bands become completely separated with a finite gap, and the system will no longer be a semimetal but a semiconductor. In this paper, we mainly focus on the semimetal phase of the system, where $\gamma < 1$.

B. Landau bands

In this paper, we consider a QW with a width L_z in the z direction, which is taken to be $L_z = 100$ nm for the numerical calculations. Applying an infinite potential $V(z) = \infty$ outside the QW, the wave vector in the z direction becomes $k_z = \pm(n_z \pi / L_z)$, with $n_z = 1, 2, 3, \dots$. In this case, the total wave function can be written as $\psi = \phi_{n_z}(z)\psi(x, y)$, where $\phi_{n_z}(z) = \sqrt{2/L_z} \sin(n_z \pi z / L_z)$ is the wave function in the z direction. In the presence of a NUMF $\mathbf{B} = [0, 0, B(x)]$, the wave vector \mathbf{k} is replaced by $\mathbf{k} \rightarrow \boldsymbol{\pi} / \hbar = \mathbf{k} + e\mathbf{A} / \hbar$ under the Peierls replacement with the Landau gauge $\mathbf{A} = (0, A_y, 0)$. Considering both electric and magnetic fields, the Hamiltonian becomes

$$\begin{aligned} \mathcal{H}_0 &= v_F(\pi_x \sigma_x + \pi_y \sigma_y) + M_n \sigma_z \\ &= \begin{bmatrix} M_n & -i\hbar v_F(\partial_x + W) \\ i\hbar v_F(-\partial_x + W) & -M_n \end{bmatrix}, \end{aligned} \quad (3)$$

where $M_n = M_a(k_c^2 - k_z^2) - (2M_a/\alpha_c^2)(n + 1/2) - \Delta_z$. Here, $\omega_c = v_F\sqrt{2}/\alpha_c$, $\alpha_c = [\hbar/eB(x)]^{1/2}$ is the magnetic length, and $W = k_y + eA_y/\hbar$ is the superpotential function [48]. In this paper, we consider two different forms of magnetic fields: uniform and non-uniform ones. We firstly present the results for the Weyl-Dirac equation $\mathcal{H}_0\psi = E\psi$, for which the Hamiltonian is shown in Eq. (3). To do that, we use the wave function for the η state $|\eta\rangle \equiv \psi = [\exp(ik_y y)/\sqrt{L_y}]\phi_{n_z}(z)\psi(x)$, where $\psi(x) = \{\psi_+(x), i\psi_-(x)\}^T$ is the wave function in the x direction, with T being the transpose operator.

1. UMF

Consider the case where a UMF $B(x) = B_0$ is applied to the system. Then we have $A_y = B_0x$. The energy levels corresponding to the Hamiltonian in Eq. (3) have three degrees of freedom $\{\eta\} = \{n, p, n_z\}$, which are given as follows, for $n \geq 1$:

$$E_\eta^u \equiv E_{n,p}^{n_z,u} = p\sqrt{n(\hbar\omega_c)^2 + M_n^2} \equiv pE_n^{n_z,u}, \quad (4)$$

where the superscript u denotes the UMF case, n and p stand for the LL and the band (conduction or valence) indices, respectively. The corresponding eigenstates are

$$\psi(x) \equiv \psi_{n,p}^{n_z,u} = \begin{bmatrix} A_{n,p}^{n_z,u} \phi_{n-1}^u(x) \\ i p B_{n,p}^{n_z,u} \phi_n^u(x) \end{bmatrix}, \quad (5)$$

where

$$\phi_n^u(x) = \frac{1}{\sqrt{2^n n! \alpha_c \sqrt{\pi}}} \exp\left[-\frac{(x-x_0)^2}{2\alpha_c^2}\right] H_n\left(\frac{x-x_0}{\alpha_c}\right) \quad (6)$$

are the normalized oscillator functions centered at $x_0 = \alpha_c^2 k_y$. The normalization coefficients are

$$A_{n,p}^{n_z,u} = \sqrt{\frac{pE_n^{n_z,u} + M_n}{2pE_n^{n_z,u}}}, \quad B_{n,p}^{n_z,u} = \sqrt{\frac{pE_n^{n_z,u} - M_n}{2pE_n^{n_z,u}}}. \quad (7)$$

For $n = 0$, $E_0^{n_z,u} = -M_0$ and $\psi_0^{n_z,u} = (0, \phi_0^u)^T$.

2. NUMF

For the NUMF, we consider an EDMF [31,37–42]:

$$B(x) = B_0 \exp\left(-\frac{x}{\lambda}\right), \quad (8)$$

where λ is the magnetic field penetration. In this case, we have $A_y = -B_0\lambda[\exp(-x/\lambda) - 1]$. Using the technique of supersymmetric quantum mechanics [31,48,49], the energy levels for the NUMF case are given by

$$E_\eta^d = E_{n,p}^{n_z,d} = p\sqrt{n\left(1 - \frac{n}{2\xi_0}\right)[\hbar\omega_c(x_0)]^2 + M_n^2}, \quad (9)$$

where $\xi_0 = \lambda k_y + eB_0\lambda^2/\hbar = [\lambda/\alpha_c(x_0)]^2$. We can see that, when $\lambda \rightarrow \infty$, $\xi_0 \rightarrow \infty$, the energy level in Eq. (9) reduces to its form of the UMF shown in Eq. (4). The corresponding eigenstates also have the same form as shown in Eq. (5) but

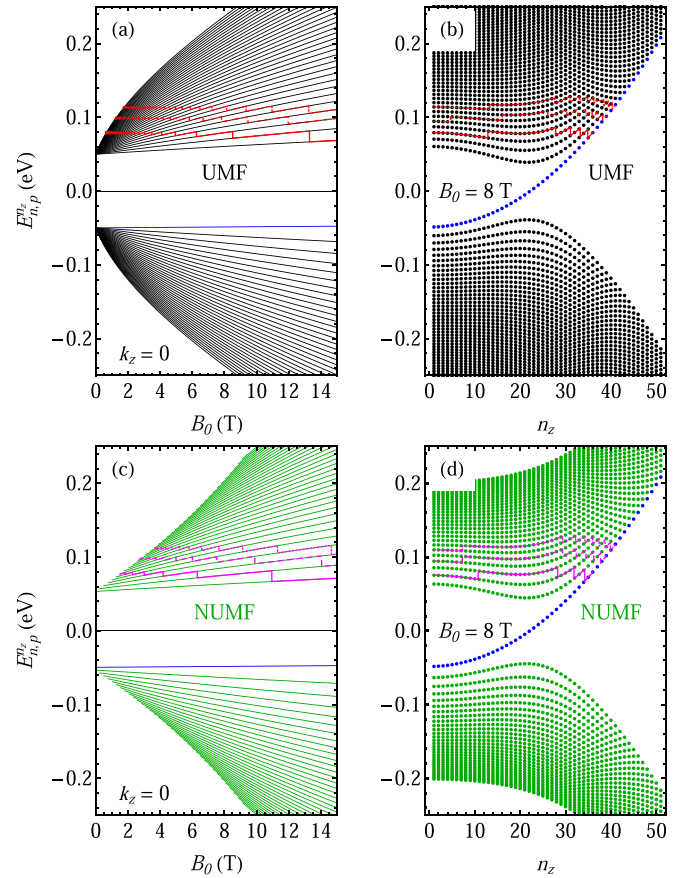


FIG. 2. (a) and (c) Landau level (LL) energy as a function of B_0 at $n_z = 1$; (b) and (d) LL energy as a function of n_z at $B_0 = 8$ T, for the uniform magnetic field (UMF) and non-UMF (NUMF) cases, respectively. The blue curves are for $n = 0$ LL. The magenta and red curves depict μ at $T = 0$ K: the solid, dashed, and dotted curves are for $n_e = n_0, 2n_0,$ and $3n_0$, respectively. The other parameters are $\gamma = 0.5$ and $\lambda = 50$ nm.

with superscript u replaced by d , and

$$\begin{aligned} \phi_n^d(x) &= \sqrt{\frac{(2\beta)n!}{\bar{\lambda}\alpha_c(x_0)(n+2\beta)!}} (2\xi_0)^\beta \exp\left(-\frac{\beta X}{\bar{\lambda}}\right) \\ &\times \exp\left[-\xi_0 \exp\left(-\frac{X}{\bar{\lambda}}\right)\right] \\ &\times L_n^{2\beta}\left[2\xi_0 \exp\left(-\frac{X}{\bar{\lambda}}\right)\right], \end{aligned} \quad (10)$$

where $\bar{\lambda} = \lambda/\alpha_c(x_0) = \sqrt{\xi_0}$, $X = (x-x_0)/\alpha_c(x_0)$, $\beta = \xi_0 - n$, and $L_n^m(x)$ are the associated Laguerre polynomials.

In Figs. 2(a) and 2(c), we show the LL energy for UMFs and NUMFs, respectively, at $n_z = 1$ as a function of B_0 . Here, we have denoted $n_0 = 5 \times 10^{23} \text{ m}^{-3}$ for convenience. In the UMF case, the LL spectrum displays a $\sqrt{B_0}$ behavior with a gap of $M_0 + M_1$, whose value is 0.1 eV at $B_0 = 0$. This feature of the LL spectrum in the WSM is like those of gapped graphene [23] or silicene [24–26] rather than transition metal dichalcogenides (TMDCs) [27–29]. Note that, in the UMF case, all the LLs start at $B_0 = 0$. Meanwhile, in the NUMF

case, the LL spectrum is also proportional to $\sqrt{B_0}$, but the LLs start at different values of B_0 , named B_{0s} . The higher the order of the LLs (i.e., the bigger the value of the LL index n), the larger the value of B_{0s} , like that in graphene [31] and black phosphorus [42]. This stems from the fact that, in the NUMF case, the number of energy levels is finite. The number of LLs, N_{\max} , is found from the condition that $[E_{n,p}^{n_z,d}]^2 < V_{\pm}(X \rightarrow \infty)$, where $V_{\pm}(X) = (\hbar v_F)^2 [W^2 \pm \partial_x W]$ is the effective potential [40], which leads to $N_{\max} = \text{Int}[\xi_0 - s\sqrt{2\xi_0}] + \delta$. Here, $s = M_0/\hbar\omega_c(x_0)$, $\text{Int}[b]$ means the integer part of b , and $\delta = 0$ (1) for the conduction (valence) band. The difference in the value of the N_{\max} in the conduction and valence bands is from the existence of the OLL, which is located in the valence band and breaks the electron-hole symmetry in the WSM. For the fixed parameters shown in Fig. 2, we have $N_{\max} = 30$ (31) at $B_0 = 8$ T for the conduction (valence) band. It should be noted that, unlike in bilayer graphene [41] and monolayer black phosphorus [42], the LLs in the WSM cannot cross each other, i.e., there is no mixing of Landau states. This can be explained as follows. Using Eq. (9), we have a condition for the intersection of two levels of LLs n_1 and n_2 , which if it occurs is $2\xi_0 = n_1 + n_2$. From that, we find the value of the magnetic field at the intersection as $B_{0c} = (\hbar/\lambda^2)(n_1 + n_2) \exp(x_0/\lambda)$, which is much smaller than that of B_{0s} (the magnetic field value where the LLs start, as mentioned above), for all values of n_1 and n_2 . That is the reason why there is no crossing between different LLs in the WSM.

In Figs. 2(b) and 2(d), we show the dispersion of the LLs along the z direction at $B_0 = 8$ T for the UMF and NUMF cases, respectively. The dispersive structure in the WSM leads to richer results in the optical transitions even in the z direction. The magenta and red curves present the μ at $n_c = n_0$ for the UMF and NUMF cases, which is defined from the

condition:

$$n_e = \int_0^{\infty} d\epsilon D(\epsilon) f(\epsilon) - \int_{-\infty}^0 d\epsilon D(\epsilon) [1 - f(\epsilon)], \quad (11)$$

where $f(\epsilon) = \{\exp[(\epsilon - \mu)/k_B T] + 1\}^{-1}$ is the distribution function, T is the temperature, n_e is the carrier density, and $D(\epsilon)$ is the density of states, which is given by

$$D(\epsilon) = \frac{g_s}{2\pi\alpha_c^2 L_z} \sum_{n,p,n_z} \delta(\epsilon - E_{n,p}^{n_z}). \quad (12)$$

Here, $g_s = 2$ is the spin degeneracy. We see that μ increases with the increase in the carrier density.

C. Magneto-optical responses

When the WSM system is excited by an incident light $\mathcal{E}(t)$ of energy $\hbar\omega$, the total Hamiltonian is written as

$$\mathcal{H} = \mathcal{H}_0 + \mathcal{H}_1, \quad (13)$$

where the unperturbed Hamiltonian part \mathcal{H}_0 is given in Eq. (3), and [28,50]

$$\mathcal{H}_1 = -\mathbf{d} \cdot \mathcal{E}(t) \quad (14)$$

is the interaction Hamiltonian part, with $\mathbf{d} = -e\mathbf{r}$ being the dipole moment operator. Here, $\mathbf{r} = (x, y, z)$ is the three-dimensional position operator. For the j direction ($j = x, y, z$), using the relation $\mathbf{d}_{\eta \rightarrow \eta'}^{j,\kappa} = \langle \eta' | \mathbf{d} | \eta \rangle = \delta_{k_y, k_y'} \delta_{n_z, n_z'} \mathbf{d}_{n,n'}^{j,\kappa}$, we have

$$\mathbf{d}_{n,n'}^{j,\kappa} = -e \frac{\langle \psi_{n',p'}^{n_z,\kappa} | [j, \mathcal{H}_0] | \psi_{n,p}^{n_z,\kappa} \rangle}{E_{\eta}^{\kappa} - E_{\eta'}^{\kappa}}, \quad (15)$$

where the superscript $\kappa = u, d$ for the UMF and NUMF, respectively. Using the commutators $[x, \mathcal{H}_0] = i\hbar v_F \sigma_x$, $[y, \mathcal{H}_0] = i\hbar v_F \sigma_y$, and $[z, \mathcal{H}_0] = -2ik_z M_a \sigma_z$, we have

$$\mathbf{d}_{n,n'}^{(x,y),\kappa} = \frac{e\hbar v_F}{\Delta E_{\eta,\eta'}^{\kappa}} \left[p A_{n',p'}^{n_z,\kappa} B_{n,p}^{n_z,\kappa} \begin{pmatrix} 1 \\ -i \end{pmatrix} \delta_{n',n+1} - p' A_{n,p}^{n_z,\kappa} B_{n',p'}^{n_z,\kappa} \begin{pmatrix} 1 \\ i \end{pmatrix} \delta_{n',n-1} \right]. \quad (16)$$

$$\mathbf{d}_{n,n'}^{z,\kappa} = \frac{2\pi i e n_z M_a}{\Delta E_{\eta,\eta'}^{\kappa} L_z} (A_{n',p'}^{n_z,\kappa} A_{n,p}^{n_z,\kappa} - p p' B_{n,p}^{n_z,\kappa} B_{n',p'}^{n_z,\kappa}) \delta_{n',n}, \quad (17)$$

where $\Delta E_{\eta,\eta'}^{\kappa} = E_{\eta}^{\kappa} - E_{\eta'}^{\kappa}$. The dipole matrix element in Eq. (16) shows that, in the (x, y) plane, only inter-LL transitions are allowed with the condition $n' - n = \pm 1$. This is in agreement with that reported in graphene [51–53], phosphorene [54], and monolayer MoS₂ [28,29]. Meanwhile, the dipole matrix element in Eq. (17) reveals that, in the z direction, only the intra-LL transitions are allowed with the condition $n' = n$, which is impossible in reality for the intraband transitions. Therefore, there is no intraband ($p = p'$) but only interband ($p \neq p'$) dipole transitions in the z direction, like the magneto-optical conductivities reported in 2D ZrTe₅ [55]. Using the equation of motion method [56,57], the electric susceptibility is calculated as follows [28]:

$$\chi_{\mu\nu}^{\kappa}(\omega) = \frac{g_s}{2\pi\epsilon_0\alpha_c^2 L_z} \sum_{n,p,n_z} \sum_{n',p'} [f(E_{\eta'}^{\kappa}) - f(E_{\eta}^{\kappa})] \times \left[\frac{(\mathbf{d}_{n,n'}^{\mu,\kappa})^* \mathbf{d}_{n,n'}^{\nu,\kappa}}{\Delta E_{\eta,\eta'}^{\kappa} + \hbar\omega + i\Gamma} + \frac{\mathbf{d}_{n,n'}^{\mu,\kappa} (\mathbf{d}_{n,n'}^{\nu,\kappa})^*}{\Delta E_{\eta,\eta'}^{\kappa} - \hbar\omega - i\Gamma} \right]. \quad (18)$$

Here, $\mu, \nu = x, y, x$, Γ is the phenomenological relaxation energy, and ϵ_0 is the vacuum permittivity. The results for the longitudinal $\chi_{xx}^{\kappa}(\omega)$ and Hall $\chi_{yx}^{\kappa}(\omega)$ susceptibilities in the (x, y) plane allow us to study the magneto-optical response for circularly polarized light, which is defined as

[28]

$$\chi_{\pm}^{\kappa}(\omega) = \chi_{xx}^{\kappa}(\omega) \pm i\chi_{yx}^{\kappa}(\omega), \quad (19)$$

where the $+/-$ signs correspond to the right/left polarization.

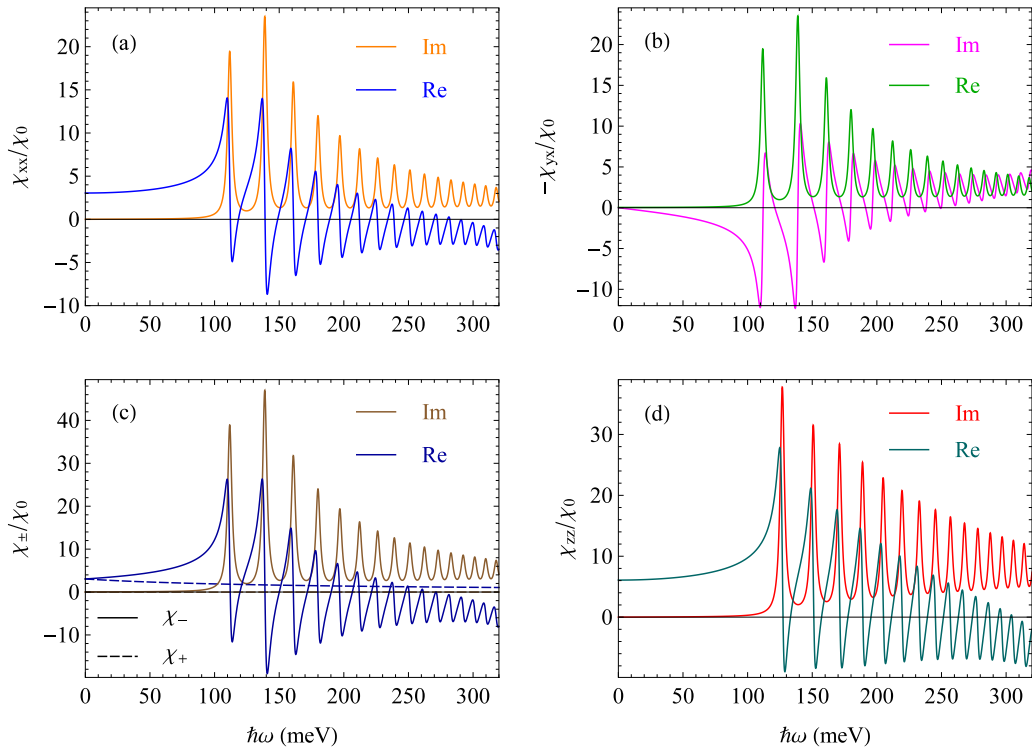


FIG. 3. The susceptibilities [in units of $\chi_0 = e^2/(\epsilon_0 L_z) \text{ eV}$] as a function of $\hbar\omega$: (a) χ_{xx} , (b) $-\chi_{yx}$, (c) χ_{\pm} , and (d) χ_{zz} . The parameters are $B = 8 \text{ T}$, $n_e = 0$, $T = 0 \text{ K}$, $\Gamma = 2 \text{ meV}$, $\gamma = 0.5$, and $\lambda = 50 \text{ nm}$.

III. RESULTS AND DISCUSSION

We now evaluate the numerical calculations for the longitudinal χ_{xx} and Hall χ_{yx} susceptibilities in the (x, y) plane and the z -direction susceptibility χ_{zz} . According to the doping level, we divide our results into two main parts: the first one is the undoped intrinsic WSM where the chemical potential lies inside the bandgap, and the second one is the doped case where the chemical potential lies in the conduction band.

A. Undoped intrinsic WSM

In the undoped case, where $n_e = 0$ and μ lies inside the gap, the magneto-optical responses (MOR) is driven by only interband transitions. In Figs. 3(a) and 3(b), the real and imaginary parts of the longitudinal χ_{xx} and Hall susceptibilities χ_{yx} , respectively, are shown as a function of incident photon energy. Since the $\text{Im}(\chi_{xx})$ and $\text{Re}(\chi_{yx})$ parts describe the absorption processes, the $\text{Re}(\chi_{xx})$ and $\text{Im}(\chi_{yx})$ parts are related to the reactive dielectric response [28], which have a close relationship with the relative refractive index changes [58,59]. Both real and imaginary parts of χ_{xx} and χ_{yx} are found to display a series of peaks. Note that, except for the first one, which is generated by only one transition $L_0 \rightarrow L_1$, each other peak appears as a composite of pair of transitions $L_{-n} \rightarrow L_{n+1}$ and $L_{-(n+1)} \rightarrow L_n$, with $n \geq 1$, where the minus sign at L_{-n} indicates that the initial LL is in the valence band. This explains that the height of the first peak is smaller than that of the second one, which is formed by a couple of transitions with $n = 1$. This result is in agreement with the half-peak feature in TMDCs [28]. Except for the first peak,

as discussed above, since the second peak, the height of the peaks decreases when the LL index increases. It can be easily understood from Eq. (9) that, when n increases, the difference in energy $\Delta E_{n,n\pm 1}^{\text{inter}} = E_n + E_{n\pm 1}$ increases, resulting in the decrease of dipole matrix element in the x direction [see Eq. (16)], resulting in a decrease in the height of peaks of χ_{xx} . Additionally, we see that, when the LL index increases, the peak spacing decreases, i.e., the peaks are getting closer and closer together. To have an insight into this result, we treat the peak spacing of two adjacent peaks $\Delta\omega_n$, from Eq. (9), as follows

$$\Delta\omega_n = E_{n+2} - E_n \propto \sqrt{(n+2)\left(1 - \frac{n+2}{2\xi_0}\right)} - \sqrt{n\left(1 - \frac{n}{2\xi_0}\right)}, \quad (20)$$

which displays as a decreasing function of n . This peak spacing behavior in WSMs is different from that in TMDCs [28,60], in which the peak spacing is found to be independent of n , and therefore, it is equal at a fixed magnetic field.

In Fig. 3(c), we show the real and imaginary parts of χ_{\pm} as a function of $\hbar\omega$. From Eq. (19), we have the following relations $\text{Im}[\chi_{\pm}] = \text{Im}[\chi_{xx}] \pm \text{Re}[\chi_{yx}]$ and $\text{Re}[\chi_{\pm}] = \text{Re}[\chi_{xx}] \pm \text{Im}[\chi_{yx}]$. We can see from Figs. 3(a) and 3(b) that $\text{Im}/\text{Re}[\chi_{xx}]$ and $\text{Re}/\text{Im}[\chi_{yx}]$ have almost the same heights and positions but with opposite signs. Therefore, in the left polarization, the contribution from $\text{Re}/\text{Im}[\chi_{yx}]$ enhances the height of the peak in $\text{Im}/\text{Re}[\chi_{xx}]$, leading to the increment of the peak in $\text{Im}/\text{Re}[\chi_{-}]$. The process is opposite to the case of right polarization. In this case, the contribution from $\text{Re}/\text{Im}[\chi_{yx}]$ reduces, even cancels, the height of the peak in

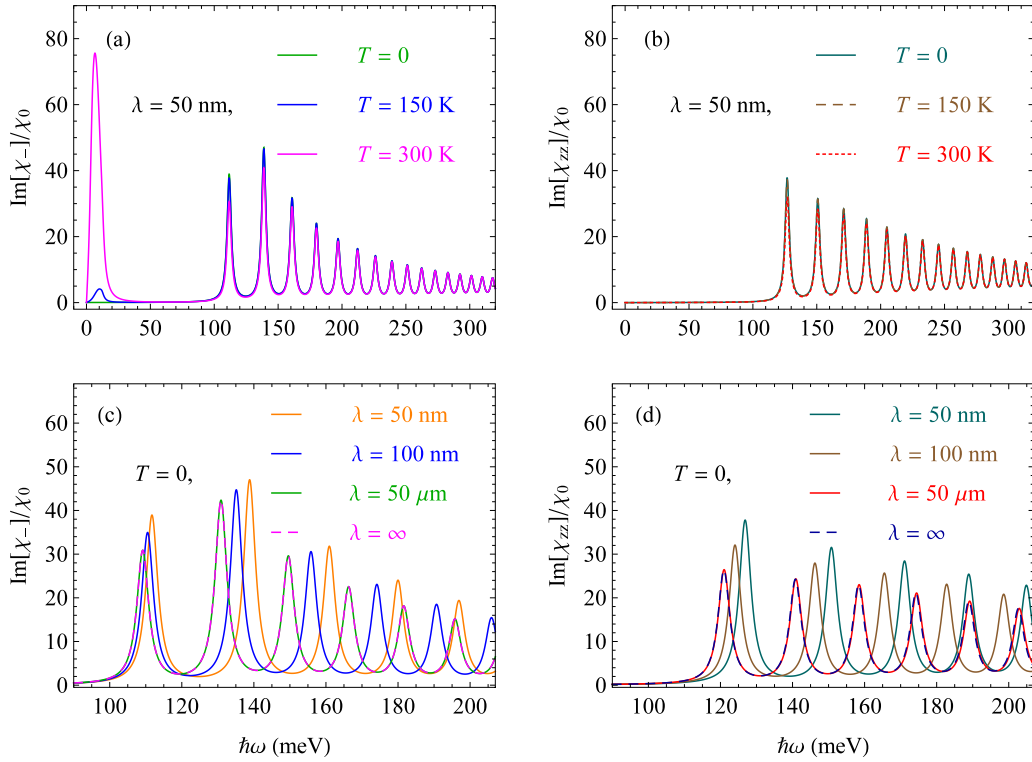


FIG. 4. The susceptibilities (in units of χ_0) as a function of $\hbar\omega$: (a) $\text{Im}[\chi_-]$ and (b) $\text{Im}[\chi_{zz}]$ for different temperatures at $\lambda = 50$ nm, (c) $\text{Im}[\chi_-]$, and (d) $\text{Im}[\chi_{zz}]$ for different λ at $T = 0$. The parameters are $B = 8$ T, $n_e = 0$, $\Gamma = 2$ meV, and $\gamma = 0.5$.

$\text{Im}/\text{Re}[\chi_{xx}]$, resulting in the disappearance of peaks in the spectrum of $\text{Im}[\chi_+]$ and $\text{Re}[\chi_+]$.

The real and imaginary parts of χ_{zz} are shown in Fig. 3(d). Like the cases of χ_{xx} , χ_{yx} , and χ_- , χ_{zz} also displays a series of peaks, where the transitions satisfy the condition $n' = n$, i.e., the peaks are formed by the transition $L_{-n} \rightarrow L_n$. Note that all peaks of the real and imaginary χ_{zz} are generated by only one transition; the half-peak feature does not exist in the z -direction susceptibility, although their height of peaks is slightly bigger than those of χ_{xx} , χ_{yx} . This is in good agreement with the results for the conductivities in WSM, where the z direction conductivity is found to be ~ 10 times bigger than that of the x -direction conductivity [5].

The effect of temperature on $\text{Im}[\chi_-]$ and $\text{Im}[\chi_{zz}]$ is shown in Figs. 4(a) and 4(b), respectively. With the increase in temperature, due to the thermal excitation, some intraband transitions become possible, resulting in the appearance of the intraband transition peaks, as observed in Fig. 4(a). The higher the temperature is, the higher the intraband absorption peaks are. For $\text{Im}[\chi_{zz}]$, due to the selection rule with the condition $n' = n$ [see Eq. (17)], all the intraband transitions are forbidden. Therefore, there are no intraband transitions observed in the z direction. The effect of the magnetic field penetration λ on $\text{Im}[\chi_-]$ and $\text{Im}[\chi_{zz}]$ is shown in Figs. 4(c) and 4(d), respectively. The case of $\lambda = \infty$ corresponds to the UMF. With the increase in λ , the peaks shift toward the lower-energy region (redshift) due to the decrease in the energy transition $\Delta E_{n,n'}^K$. We can also see that the curves with $\lambda = 50$ μm almost coincide with those of $\lambda = \infty$. It shows that, in practice, for magnetic field penetration of $\lambda = 50$ μm , the NUMF can be considered as the UMF.

B. Doped WSM

We now turn our attention to the doped WSM case, where $n_e \neq 0$, and therefore, μ lies in the conduction band. In this case, both intraband and interband transitions are possible. As we can see from Figs. 3 and 4, the behavior of χ_{zz} is almost like that of χ_- . In this subsection, we mainly focus on χ_- .

1. Intraband transitions

In Fig. 5, we present the effect of the temperature, electron density, magnetic field penetration, and electric field (recall that $\gamma = \Delta_z/M_a k_c^2$) on the imaginary and real parts of χ_- due to the intraband transitions. Because the energy transition $\Delta E_{n,n'}$ in the intraband transitions is very small, we chose a value of Γ to be $\Gamma = 0.2$ meV, which is smaller than LL spacing for the peaks that are observable. Overall, the energy scale (the spectra weight) of the intraband transition peaks is much smaller (bigger) than those of the interband ones, agreeing with that in TMDCs [28] and graphene [61]. This is because, in the intraband transitions, the energy scale is determined by $\Delta E_{n,n\pm 1}^{\text{intra}} = |E_{n\pm 1} - E_n|$, which is much smaller than that of the interband transitions $\Delta E_{n,n\pm 1}^{\text{inter}} = E_{n\pm 1} + E_n$. Meanwhile, the high spectra weight of the intraband transition peaks is the result of two main reasons. The first one is from its small energy transition scale, as mentioned above (recall that the values of $\text{Im}[\chi_-]$ and $\text{Re}[\chi_-]$ are proportional to $(\Delta E_{n,n\pm 1}^{\text{intra}})^{-1}$). The second is from the small value of Γ , which is chosen so we can observe the intraband transition peaks.

In Fig. 5(a), we show the temperature effect on $\text{Im}[\chi_-]$ and $\text{Re}[\chi_-]$ at $n_e = n_0$, $\lambda = 50$ nm, and $\gamma = 0.5$, where μ

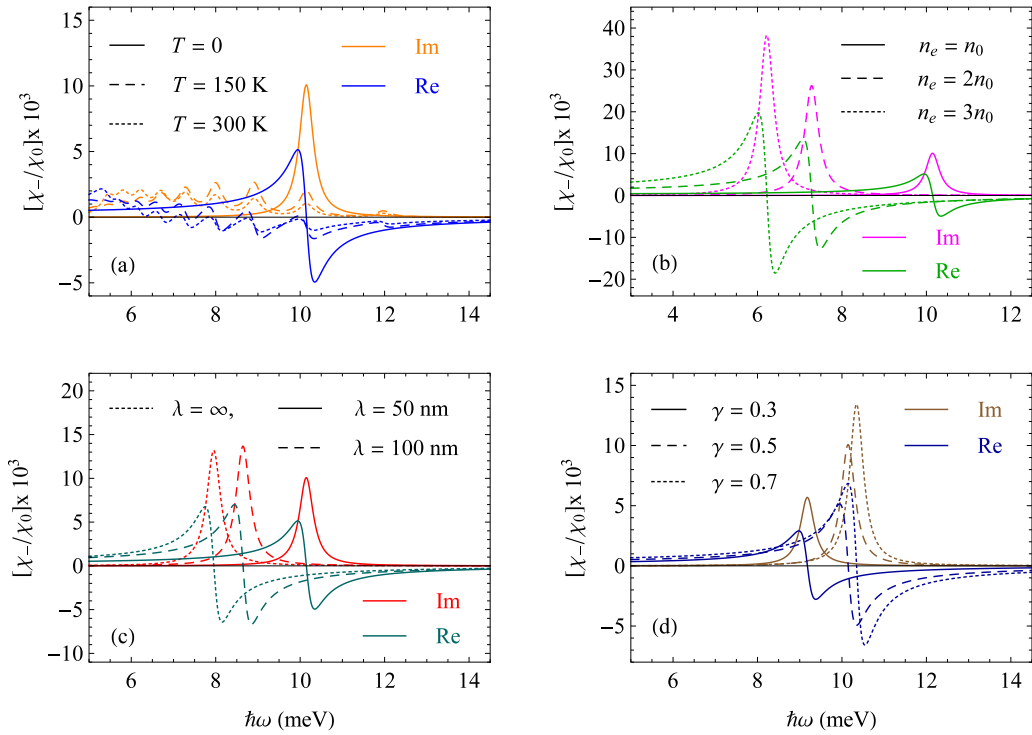


FIG. 5. $\text{Im}[\chi_-]$ and $\text{Re}[\chi_-]$ (in units of χ_0) due to intraband transitions as a function of $\hbar\omega$ at $B = 8$ T and $\Gamma = 0.2$ meV: (a) for several T , (b) for several n_e , (c) for several λ , and (d) for several γ . The parameters are $T = 0$, $n_e = n_0$, $\lambda = 50$ nm, and $\gamma = 0.5$ except for otherwise indicated.

lies between L_2 and L_3 [see Fig. 2(a)]. Therefore, at $T = 0$, only intraband transition $L_2 \rightarrow L_3$, with photon energy $\hbar\omega_{2,3} = 10.15$ meV, is allowed, while the other transitions are blocked, caused by the Pauli blocking. With the increase in T , some LLs below the chemical potential (L_0 , L_1 , and L_2) become thermally depopulated and no longer completely occupied. Consequently, electrons in the LLs below can jump to fill these vacancies, generating some new intraband transitions. Here, we can observe the new intraband transition $L_1 \rightarrow L_2$ at $\hbar\omega_{1,2} = 11.97$ meV. Meanwhile, the LLs above μ ($L_{n \geq 3}$) become no longer fully empty due to the thermal population. These thermally populated electrons can jump to higher LLs to generate new peaks, which are the results of the $L_n \rightarrow L_{n+1}$ transitions with $n \geq 3$. All these peaks are located in the lower-energy region in comparison with the main peak ($L_2 \rightarrow L_3$). These results are in good agreement with those in graphene [61] and topological insulator thin films [62].

In Fig. 5(b), we show the electron concentration effect on $\text{Im}[\chi_-]$ and $\text{Re}[\chi_-]$ at $T = 0$, $\lambda = 50$ nm, and $\gamma = 0.5$. We can see from Fig. 2(a) that, when n_e increases, the chemical potential shifts upward, resulting in the change in the allowed transitions. The allowed intraband transitions and their corresponding energies are listed in the first three columns of Table I, which are read as follows. For $n_e = n_0$ ($2n_0, 3n_0$), μ lies between $L_{2(5,7)}$ and $L_{3(6,8)}$, leading to the allowed transition being $L_n \rightarrow L_{n+1}$, with $n = 2$ (5, 7), generating a peak at $\hbar\omega = 10.15$ (7.28, 6.22) meV. With the increase in n_e , the peaks shift to the lower-energy region and enhance their height. It is clear from Table I that, when n_e increases, the LL index of allowed transitions n increases, leading to a decrease

in the difference in energy:

$$\Delta E_{n,n\pm 1}^{\text{intra}} = |E_{n\pm 1} - E_n| \propto \left| \sqrt{(n \pm 1) \left(1 - \frac{n \pm 1}{2\xi_0}\right)} - \sqrt{n \left(1 - \frac{n}{2\xi_0}\right)} \right|, \quad (21)$$

because the $\Delta E_{n,n\pm 1}^{\text{intra}}$ shown in Eq. (21) is a descending function of n .

The effect of the magnetic field penetration λ on $\text{Im}[\chi_-]$ and $\text{Re}[\chi_-]$ is shown in Fig. 5(c). The varying λ also leads to the change of the position of μ and therefore also changes the LL order involved in the allowed transition. The allowed transitions and their corresponding energies are listed in the central three columns of Table I. In the case of $\lambda = 50$ nm, the transition is $L_2 \rightarrow L_3$, while it is $L_3 \rightarrow L_4$ for both cases of $\lambda = 100$ nm and $\lambda = \infty$ (UMF). Note that, although the allowed transitions in the two cases of $\lambda = 100$ nm and UMF have the same LL index ($n = 3$), their energy transitions are different. This is because the change in λ also leads to the change in the energy spectrum [see Eq. (9)], which leads to the

TABLE I. List of allowed intraband transitions $L_n \rightarrow L_{n+1}$ and their corresponding energies (in units of meV) for different n_e , λ , and γ from Figs. 5(b), 5(c), and 5(d).

n_e	n	$\hbar\omega$	λ	n	$\hbar\omega$	γ	n	$\hbar\omega$
n_0	2	10.15	50 nm	2	10.15	0.3	1	9.18
$2n_0$	5	7.28	100 nm	3	8.65	0.5	2	10.15
$3n_0$	7	6.22	∞	3	7.95	0.7	3	10.35

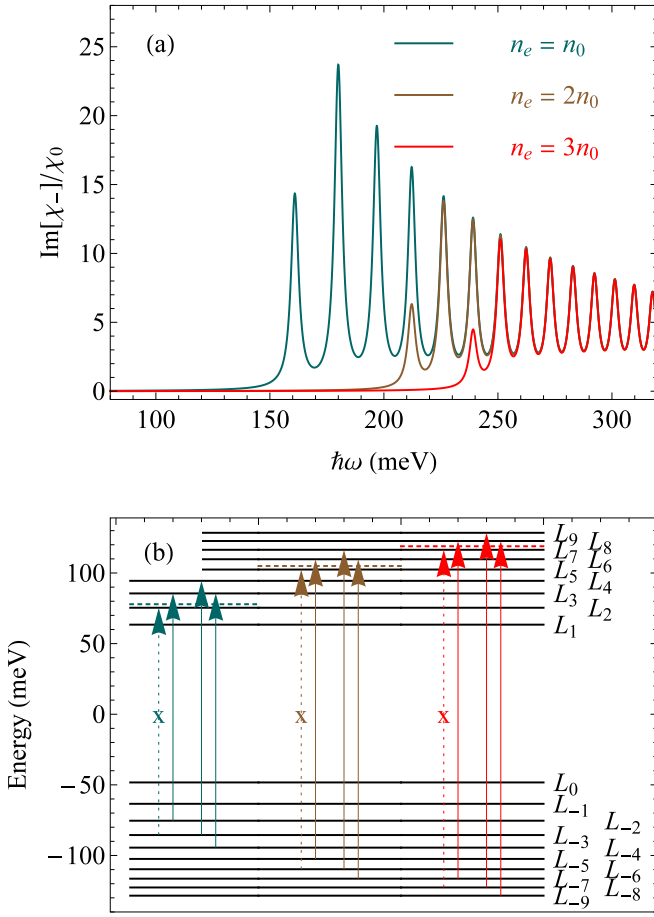


FIG. 6. (a) $\text{Im}[\chi_-]$ (in units of χ_0) due to interband transitions vs $\hbar\omega$ for different n_e . (b) Scheme of optical interband transitions, where the dotted lines show the corresponding chemical potentials. The parameters are $B = 8$ T, $\Gamma = 2$ meV, $T = 0$, $\lambda = 50$ nm, and $\gamma = 0.5$.

change in the $\Delta E_{n,n\pm 1}^{\text{intra}}$. Like Fig. 4(c), when the λ increases, the intraband transition peaks also redshift due to the decrease of $\Delta E_{n,n\pm 1}^{\text{intra}}$.

The effect of the electric field, expressed in terms of γ , on $\text{Im}[\chi_-]$ and $\text{Re}[\chi_-]$ is illustrated in Fig. 5(d). Like the electron density and magnetic field penetration, the varying electric field also changes the position of μ leading to the change of the allowed transition, as listed in the last three columns of Table I. With the increase in the electric field, the intraband transition peaks show a blueshift due to the increase of $\Delta E_{n,n\pm 1}^{\text{intra}}$.

2. Interband transitions

In Fig. 6(a), we show $\text{Im}[\chi_-]$ due to interband transitions vs $\hbar\omega$ for different electron densities. Here, $\text{Im}[\chi_-]$ due to interband transitions also displays a series of peaks. Due to the Pauli blocking, where all transitions which have the final LLs below μ are forbidden, the first peaks of each series (threshold energy) locate at different positions depending on the position of μ . The increase in n_e pushes μ upward, resulting in the increase in the LL index involved in the transitions. Therefore, the threshold energy shifts to a higher-energy region. This

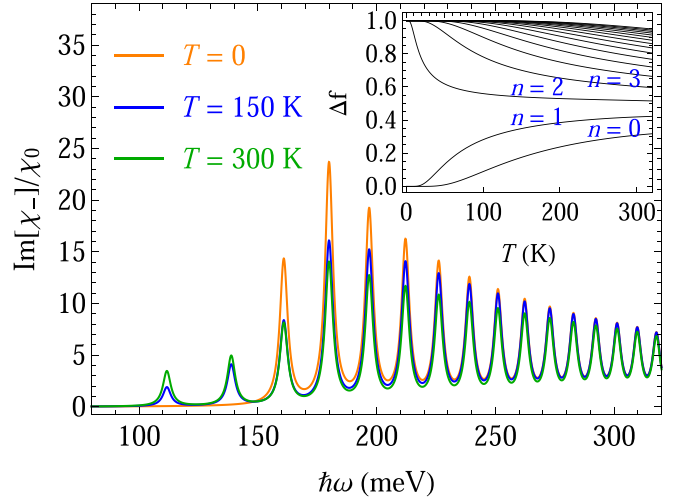


FIG. 7. $\text{Im}[\chi_-]$ (in units of χ_0) due to interband transitions as a function of $\hbar\omega$ for different temperature. The inset shows $\Delta f = |f_{-n} - f_{n+1}|$ as a function of temperature. The parameters are $B = 8$ T, $\Gamma = 2$ meV, $n_e = n_0$, $\lambda = 50$ nm, and $\gamma = 0.5$.

is illustrated visually in the scheme of Fig. 6(b), where the dotted arrows (with an x sign on them) illustrate the forbidden transitions. For example, for $n_e = n_0$, μ lies between L_2 and L_3 , and the first transition is from L_{-2} to L_3 [which is illustrated by the first cyan solid arrow in Fig. 6(b)], while its counterpart ($L_{-3} \rightarrow L_2$) is forbidden (which is illustrated by the cyan dotted arrow). This transition forms the first peak in the series of peaks of the case of $n_e = n_0$ (cyan curve) in Fig. 6(a). Its second peak is derived from a pair of transitions $L_{-3} \rightarrow L_4$ and $L_{-4} \rightarrow L_3$, which are illustrated by the second and third cyan solid arrows in Fig. 6(b). Similarly, the third one is from $L_{-4} \rightarrow L_5$ and $L_{-5} \rightarrow L_4$, and so on. Cases of $n_e = 2n_0$ and $n_e = 3n_0$ can also be expressed in the same way. Additionally, the half-peak feature is still observed in the interband transitions. This half-peak feature is in agreement with that obtained in TI thin film [62,63] and the half-plateau characteristic in TMDC monolayers [28]. In Fig. 7, we show the imaginary part of χ_- due to interband transitions as a function of $\hbar\omega$ at $B = 8$ T, $\Gamma = 2$ meV, $n_e = n_0$, $\lambda = 50$ nm, and $\gamma = 0.5$ for different temperatures. Like the undoped case [see Fig. 4(a)], in the doped case, $\text{Im}[\chi_-]$ also displays a series of peaks. However, unlike in the undoped case where all the interband transitions are allowed, in the doped case, not all but only interband transitions whose final LLs above μ are allowed, as discussed in Fig. 6. With parameters used in Fig. 7, μ lies between L_2 and L_3 . Therefore, at $T = 0$, all transitions which have final LLs indexes < 2 are blocked, and the allowed transitions start at $n = 2$ (see again the case of $n_e = n_0$ in Fig. 6). When the temperature increases, due to the thermal excitation, a couple of new interband transitions whose final LLs below μ become possible, form new interband transitions peaks, as observed clearly from the blue and green curves of Fig. 7 for $T = 150$ and 300 K, respectively. In addition to generating new peaks, thermal excitation affects the height of peaks. This effect is not similar for all transitions but depends on the position of their final LLs. (i) For the transitions which have their final LLs below μ (including

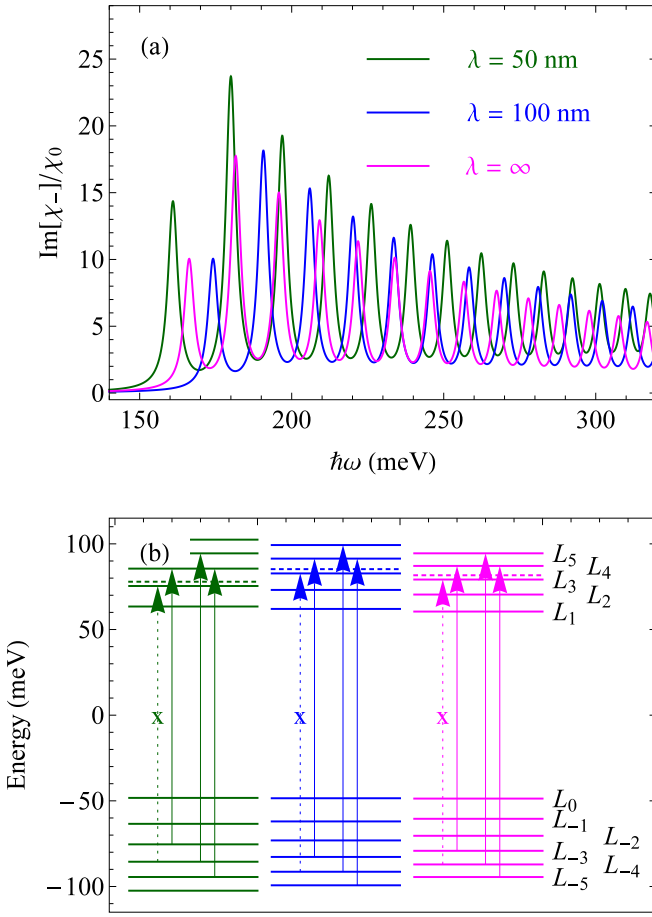


FIG. 8. (a) $\text{Im}[\chi_-]$ (in units of χ_0) due to interband transitions vs $\hbar\omega$ for different λ . (b) Scheme of optical interband transitions where the dotted lines show the chemical potentials. The parameters are $B = 8$ T, $\Gamma = 2$ meV, $T = 0$, $n_e = n_0$, and $\gamma = 0.5$.

$n = 0$ and 1), the height of peaks increases with the increase in the temperature. Note that these two peaks are formed due to the thermal excitation and appear only in the case of $T \neq 0$. When the LLs L_0 and L_1 are thermally depopulated, electrons in these LLs get thermal energy and jump to higher levels, creating holes in there. As a result, other electrons in the valence band can jump in to fill those holes. The higher the temperature, the stronger thermal excitation occurs, leading to an increase in the probability of transitions, which in turn leads to an enhancement of the peak height. (ii) Meanwhile, for the transitions whose final LLs are above μ , the height of the peaks decreases with the temperature. In this case, the LLs are thermally populated and partially occupied. The higher the temperature, the more thermal electrons will appear there, leading to the decrease in the probability of transitions, therefore resulting in the reduction in the height of peaks. Mathematically, note from Eq. (18) that $\chi(\omega)$ is proportional to $\Delta f = f(E_{\eta}^k) - f(E_{\eta}^k)$, which increases with temperature when $n < 2$ and decreases with the temperature when $n \geq 2$, as shown clearly in the inset.

The effect of λ on $\text{Im}[\chi_-]$ is depicted in Figs. 8(a) and 8(b). We can see from Fig. 8(b) that the varying λ not only changes the energy spectrum but also changes the position

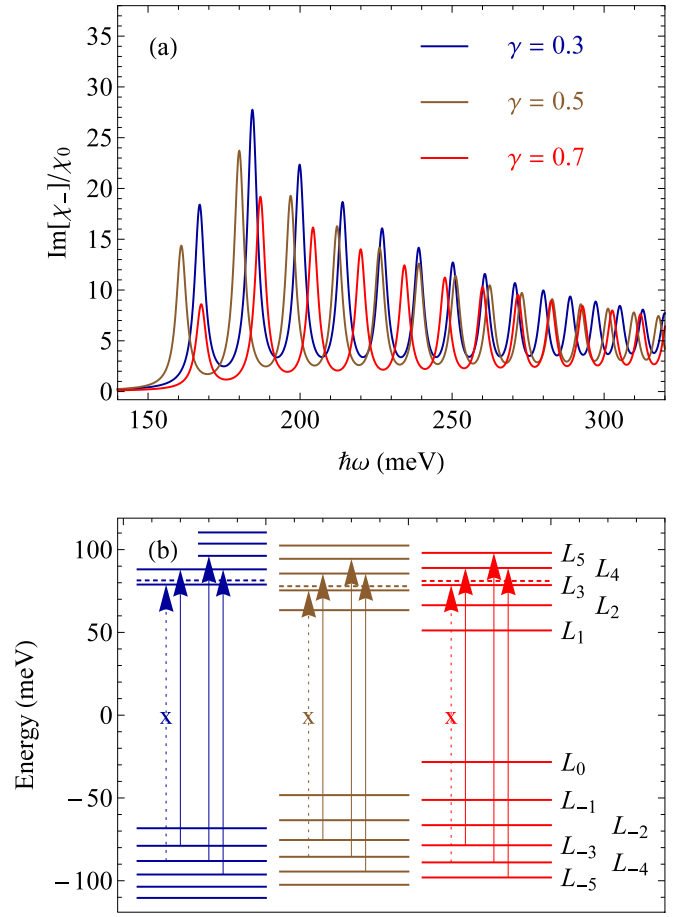


FIG. 9. (a) $\text{Im}[\chi_-]$ (in units of χ_0) due to interband transitions vs $\hbar\omega$ for different electric fields. (b) Scheme of optical interband transitions where the dotted lines show the chemical potentials. The parameters are $B = 8$ T, $\Gamma = 2$ meV, $T = 0$, $\lambda = 50$ nm, and $n_e = n_0$.

of the chemical potential, therefore changing the threshold energy. When λ increases, the E_{η}^d slightly reduces, resulting in the reduction in the difference in energy, which leads to the redshift behavior of the peak positions. Note that the redshift behavior is only valid for transitions with the same LL index n . The first peak in the case of $\lambda = 50$ nm corresponds to the transition $L_{-2} \rightarrow L_3$, while it is $L_{-3} \rightarrow L_4$ in both rest cases [see the scheme in Fig. 8(b)]. Since $\hbar\omega_{n,n\pm 1} = \Delta E_{n,n\pm 1}^{\text{inter}}$, with

$$\begin{aligned} \Delta E_{n,n\pm 1}^{\text{inter}} &= E_{n\pm 1} + E_n \\ &\propto \sqrt{(n \pm 1) \left(1 - \frac{n \pm 1}{2\xi_0}\right)} + \sqrt{n \left(1 - \frac{n}{2\xi_0}\right)} \quad (22) \end{aligned}$$

being an increasing function of n , the first peak of the case $\lambda = 50$ nm (which has $n = 2$) lies on the left-hand side of the first peaks of the cases $\lambda = 100$ nm and $\lambda = \infty$ (both have $n = 3$).

Finally, the electric field effect on $\text{Im}[\chi_-]$ is illustrated in Figs. 9(a) and 9(b). The varying λ also changes the energy spectrum and the position of μ , therefore changing the threshold energy. When γ increases, E_{η}^d reduces, resulting in the reduction in the transition energy, but μ increases, resulting in the increase of the energy threshold. This competition leads

to a complicated change in the peak positions of the interband transitions with the varying of the electric field.

IV. CONCLUSIONS

We have studied the LLs and the optical properties of a WSM QW in the presence of a NUMF with an exponential decaying form. We have analyzed in detail the effect of the magnetic field penetration, a quantity that characterizes the exponential decaying magnetic field, on the LL energy spectrum in both the (x, y) plane and the z direction. Unlike in the UMF case, in the NUMF, (i) the LLs do not start at $B_0 = 0$ but at B_{0s} ; the higher the LL index, the bigger the value of B_{0s} ; (ii) the number of energy levels is finite. Additionally, the LLs in the WSM do not cross each other, and therefore, there is no mixing of Landau states. When $\lambda \rightarrow \infty$, the energy level of the NUMF reduces to its form of the UMF.

The selection rules obtained from the dipole matrix element show that, in the (x, y) plane, only inter-LL transitions are allowed with the condition $n' = n \pm 1$, which is valid for

both intraband and interband transitions. Meanwhile, in the z direction, only the intra-LL transitions are allowed with the condition $n' = n$. Consequently, there is no intraband but only interband transitions in the z direction.

We have also analyzed in detail the longitudinal and Hall optical response under the effect of the temperature, the magnetic field penetration, the electron density, and the electric field in both doped and undoped cases. Except for the case of intraband transition at $T = 0$, in all other cases, both real and imaginary parts of the longitudinal and Hall susceptibilities, χ_- displays a series of peaks where the height of peaks and the peak spacing decrease with the increase of the LL index. The temperature significantly affects the optical response. The increase in the temperature triggers new transitions, forming new peaks in the optical response spectrum. The electron density, magnetic field penetration, and electric field all markedly affect the position of the chemical potential; therefore, the change in these parameters strongly affects the value of the threshold energy. In this paper, we provide an effective way to control the threshold energy and therefore to control the optical response spectrum in the WSM.

-
- [1] X. Wan, A. M. Turner, A. Vishwanath, and S. Y. Savrasov, *Phys. Rev. B* **83**, 205101 (2011).
- [2] A. A. Burkov and L. Balents, *Phys. Rev. Lett.* **107**, 127205 (2011).
- [3] B. Singh, A. Sharma, H. Lin, M. Z. Hasan, R. Prasad, and A. Bansil, *Phys. Rev. B* **86**, 115208 (2012).
- [4] S. Murakami, *New J. Phys.* **9**, 356 (2007).
- [5] H.-Z. Lu, S.-B. Zhang, and S.-Q. Shen, *Phys. Rev. B* **92**, 045203 (2015).
- [6] H. Yu, L. Sheng, and D. Y. Xing, *EPL* **130**, 47004 (2020).
- [7] A. A. Zyuzin, S. Wu, and A. A. Burkov, *Phys. Rev. B* **85**, 165110 (2012).
- [8] S. M. Young, S. Zaheer, J. C. Y. Teo, C. L. Kane, E. J. Mele, and A. M. Rappe, *Phys. Rev. Lett.* **108**, 140405 (2012).
- [9] Z. K. Liu, B. Zhou, Y. Zhang, Z. J. Wang, H. M. Weng, D. Prabhakaran, S.-K. Mo, Z. X. Shen, Z. Fang, X. Dai *et al.*, *Science* **343**, 864 (2014).
- [10] S. Borisenko, Q. Gibson, D. Evtushinsky, V. Zabolotnyy, B. Büchner, and R. J. Cava, *Phys. Rev. Lett.* **113**, 027603 (2014).
- [11] S.-M. Huang, S.-Y. Xu, I. Belopolski, C.-C. Lee, G. Chang, B. Wang, N. Alidoust, G. Bian, M. Neupane, C. Zhang *et al.*, *Nat. Commun.* **6**, 7373 (2015).
- [12] H. Weng, C. Fang, Z. Fang, B. A. Bernevig, and X. Dai, *Phys. Rev. X* **5**, 011029 (2015).
- [13] X. Su-Yang, B. Ilya, A. Nasser, N. Madhab, B. Guang, Z. Chenglong, S. Raman, C. Guoqing, Y. Zhujun, L. Chi-Cheng *et al.*, *Science* **349**, 613 (2015).
- [14] C. Shekhar, A. K. Nayak, Y. Sun, M. Schmidt, M. Nicklas, I. Leermakers, U. Zeitler, Y. Skourski, J. Wosnitza, Z. Liu *et al.*, *Nat. Phys.* **11**, 645 (2015).
- [15] S. Jeon, B. B. Zhou, A. Gyenis, B. E. Feldman, I. Kimchi, A. C. Potter, Q. D. Gibson, R. J. Cava, A. Vishwanath, and A. Yazdani, *Nat. Mater.* **13**, 851 (2014).
- [16] P. E. C. Ashby and J. P. Carbotte, *Phys. Rev. B* **87**, 245131 (2013).
- [17] J. M. Shao and G. W. Yang, *AIP Adv.* **6**, 025312 (2016).
- [18] S.-B. Zhang and J. Zhou, *Phys. Rev. B* **101**, 085202 (2020).
- [19] J.-M. Parent, R. Côté, and I. Garate, *Phys. Rev. B* **102**, 245126 (2020).
- [20] S. Vadrnais and R. Côté, *Phys. Rev. B* **104**, 144409 (2021).
- [21] S. Bertrand, J.-M. Parent, R. Côté, and I. Garate, *Phys. Rev. B* **100**, 075107 (2019).
- [22] N. P. Armitage, E. J. Mele, and A. Vishwanath, *Rev. Mod. Phys.* **90**, 015001 (2018).
- [23] P. M. Krstajić and P. Vasilopoulos, *Phys. Rev. B* **86**, 115432 (2012).
- [24] C. J. Tabert and E. J. Nicol, *Phys. Rev. Lett.* **110**, 197402 (2013).
- [25] D. Muoi, N. N. Hieu, C. V. Nguyen, B. D. Hoi, H. V. Nguyen, N. D. Hien, N. A. Poklonski, S. S. Kubakaddi, and H. V. Phuc, *Phys. Rev. B* **101**, 205408 (2020).
- [26] H. T. T. Nguyen, L. Dinh, T. V. Vu, L. T. Hoa, N. N. Hieu, C. V. Nguyen, H. V. Nguyen, S. S. Kubakaddi, and H. V. Phuc, *Phys. Rev. B* **104**, 075445 (2021).
- [27] H. Ochoa and R. Roldán, *Phys. Rev. B* **87**, 245421 (2013).
- [28] G. Catarina, J. Have, J. Fernández-Rossier, and N. M. R. Peres, *Phys. Rev. B* **99**, 125405 (2019).
- [29] N. D. Hien, C. V. Nguyen, N. N. Hieu, S. S. Kubakaddi, C. A. Duque, M. E. Mora-Ramos, L. Dinh, T. N. Bich, and H. V. Phuc, *Phys. Rev. B* **101**, 045424 (2020).
- [30] S.-B. Zhang, H.-Z. Lu, and S.-Q. Shen, *New J. Phys.* **18**, 053039 (2016).
- [31] S. Kuru, J. Negro, and L. M. Nieto, *J. Phys.: Condens. Matter* **21**, 455305 (2009).
- [32] C. A. Downing and M. E. Portnoi, *Phys. Rev. B* **94**, 045430 (2016).
- [33] D. Sidler, V. Rokaj, M. Ruggenthaler, and A. Rubio, *arXiv:2201.05069* (2022).
- [34] A. Nogaret, *J. Phys.: Condens. Matter* **22**, 253201 (2010).
- [35] J. Eisenstein, *Rev. Mod. Phys.* **26**, 277 (1954).

- [36] M. L. Leadbeater, C. L. Foden, J. H. Burroughes, M. Pepper, T. M. Burke, L. L. Wang, M. P. Grimshaw, and D. A. Ritchie, *Phys. Rev. B* **52**, R8629 (1995).
- [37] A. Raya and E. Reyes, *Phys. Rev. D* **82**, 016004 (2010).
- [38] N. Sadooghi and F. Taghinavaz, *Phys. Rev. D* **85**, 125035 (2012).
- [39] K. Handrich, *Phys. Rev. B* **72**, 161308(R) (2005).
- [40] T. K. Ghosh, *J. Phys.: Condens. Matter* **21**, 045505 (2009).
- [41] D. Wang and G. Jin, *Phys. Lett. A* **377**, 2901 (2013).
- [42] D. Wang, A. Shen, J.-P. Lv, and G. Jin, *J. Phys.: Condens. Matter* **32**, 095301 (2020).
- [43] M. Ezawa, *New J. Phys.* **14**, 033003 (2012).
- [44] G.-B. Liu, W.-Y. Shan, Y. Yao, W. Yao, and D. Xiao, *Phys. Rev. B* **88**, 085433 (2013).
- [45] H.-Z. Lu, W.-Y. Shan, W. Yao, Q. Niu, and S.-Q. Shen, *Phys. Rev. B* **81**, 115407 (2010).
- [46] K.-Y. Yang, Y.-M. Lu, and Y. Ran, *Phys. Rev. B* **84**, 075129 (2011).
- [47] M. Ezawa, *Phys. Rev. Lett.* **109**, 055502 (2012).
- [48] B. Midya and D. J. Fernández, *J. Phys. A: Math. Theor.* **47**, 285302 (2014).
- [49] F. Cooper, A. Khare, and U. Sukhatme, *Phys. Rep.* **251**, 267 (1995).
- [50] J. Have, G. Catarina, T. G. Pedersen, and N. M. R. Peres, *Phys. Rev. B* **99**, 035416 (2019).
- [51] V. P. Gusynin, S. G. Sharapov, and J. P. Carbotte, *Phys. Rev. Lett.* **98**, 157402 (2007).
- [52] M. Koshino and T. Ando, *Phys. Rev. B* **77**, 115313 (2008).
- [53] H. V. Phuc and N. N. Hieu, *Opt. Commun.* **344**, 12 (2015).
- [54] C. V. Nguyen, N. N. Hieu, C. A. Duque, D. Q. Khoa, N. V. Hieu, L. V. Tung, and H. V. Phuc, *J. Appl. Phys.* **121**, 045107 (2017).
- [55] Y.-X. Wang and F. Li, *Phys. Rev. B* **101**, 195201 (2020).
- [56] A. Ferreira, J. Viana-Gomes, Y. V. Bludov, V. Pereira, N. M. R. Peres, and A. H. Castro Neto, *Phys. Rev. B* **84**, 235410 (2011).
- [57] N. M. R. Peres, R. M. Ribeiro, and A. H. Castro Neto, *Phys. Rev. Lett.* **105**, 055501 (2010).
- [58] C. V. Nguyen, N. N. Hieu, D. Muoi, C. A. Duque, E. Feddi, H. V. Nguyen, L. T. T. Phuong, B. D. Hoi, and H. V. Phuc, *J. Appl. Phys.* **123**, 034301 (2018).
- [59] P. T. Huong, D. Muoi, T. N. Bich, H. V. Phuc, C. A. Duque, P. T. N. Nguyen, C. V. Nguyen, N. N. Hieu, and L. T. Hoa, *Physica E* **124**, 114315 (2020).
- [60] M. Tahir and P. Vasilopoulos, *Phys. Rev. B* **94**, 045415 (2016).
- [61] B. Scharf, V. Perebeinos, J. Fabian, and I. Žutić, *Phys. Rev. B* **88**, 125429 (2013).
- [62] N. V. Hieu, S. S. Kubakaddi, N. N. Hieu, and H. V. Phuc, *J. Phys.: Condens. Matter* **34**, 305702 (2022).
- [63] K. Rahim, A. Ullah, M. Tahir, and K. Sabeeh, *J. Phys.: Condens. Matter* **29**, 425304 (2017).